Spatially-dependent modeling and simulation of runaway electron mitigation in DIII-D

M. T. Beidler,* D. del-Castillo-Negrete, L. Baylor, D. Shiraki, and D. A. Spong
Oak Ridge National Laboratory, Oak Ridge, Tennessee 37831-8071, USA

Confinement of runaway electrons (REs) plays a potential key role in the efficiency of impurity-based mitigation strategies. This work analyzes a DIII-D discharge that injects Ne gas to dissipate a post-disruption, RE beam. The kinetic RE code KORC has been enhanced to incorporate experimentally-reconstructed, time-dependent magnetic and electric fields, and line integrated electron density data to construct spatiotemporal models of electron and partially-ionized impurity transport in the companion plasma. Simulations indicate that the observed current dissipation is mostly due to deconfinement losses to the wall, and not to collisional slowing down. We posit that the deconfinement of REs is caused by current profile changes lowering the rotational transform due to increased pitch angle scattering of REs by injected impurities. Comparisons of experimental current evolution and KORC results are performed including Coulomb collisions with partially-ionized impurity physics, different models of initial RE energy and pitch angle distributions, and different spatiotemporal electron and partially-ionized impurity transport. The majority of KORC simulations indicate that while the RE beam current is decreasing, the RE beam energy increases due to induced electric field acceleration until confinement degrades. This research provides an initial quantification of the efficacy of RE mitigation via injected impurities, and identification of the critical role played by loss of confinement as compared to the relatively slow collisional damping.

I. INTRODUCTION

If not avoided or dissipated, runaway electrons (REs) can seriously damage ITER's plasma-facing components [1, 2]. If avoidance fails, shattered pellet injection (SPI) is the leading candidate to dissipate REs in ITER [3–6], and although significant progress has been made, there is a pressing need for modeling and simulation studies to assess the efficacy of SPI and to optimize different dissipation strategies, such as massive gas injection (MGI). From the theory and simulation perspective, there is a need to develop and validate realistic models of the interaction of REs with partially-ionized impurities, such as those proposed in Refs. [7, 8].

Recent experiments at DIII-D indicate that SPI and MGI perform similarly [9]. This work will focus on DIII-D experiment #164409, which has been reported extensively in Ref. [9]. The evolution of characteristic parameters are plotted in Fig. 1. At approximately 1.2 s, a small Ar pellet is injected that triggers the observed current quench in Fig. 1a. A RE beam is generated and position controlled until a secondary injection of Ne gas causes the RE beam to dissipate. Figure 1b shows the three vertical, interferometer chords, capturing the evolution of line integrated electron density. Figure 1c calculated the toroidal electric field consistent with the loop voltage measured at the high field side (HFS) and low field side (LFS). The bremsstrahlung hard x-ray (HXR) signals in Fig.1d are measured by a bismuth-germanate based scintillator located at the bottom of DIII-D and mostly sensitive to $1-10,\mathrm{MeV}$ photons [10]. The RE plateau phase is significantly different from the pre-thermal quench (TQ), in that the majority of the current is carried by REs and the "companion", or background, plasma plays a minor role in the dynamics. For this reason, the dynamics during this phase can be well studied using a particle tracking code, and in this work we employ the Kinetic Orbit Runaway electrons Code (KORC) [11].

There have been significant previous efforts to model RE dissipation by impurity injection. Refs. [12–14] use 1D transport codes with Fokker-Planck models for REs having physics of bound electrons and partially-ionized impurities. Ref. [15] uses ESTAR modeling of the Bethe stopping power of an idealized beam of REs in JET-ILW. Refs. [16, 17] use guiding center test particle modeling using KORCGC, a predecessor of KORC, with 2D axisymmetric fields and Monte Carlo collision operators having physics of bound electrons and partially-ionized impurities with constant density profiles.

Several studies using guiding center test particle modeling have also been employed to study RE generation and confinement during the thermal quench of a disruption. Refs. [18, 19] use the ANTS code to evolve particle orbits in 3D fields. Refs. [20, 21] use the RE orbit module in JOREK to calculate RE confinement and hot tail and Dreicer generation during a simulated thermal quench. Ref. [22] uses the RE orbit module in NIMROD to calculate RE confinement during impurity injection induced thermal quench and Ref. [23] uses the same module to calculate RE confinement with a pre-seeded large-scale island structure. Ref.[24] uses a RE orbit module with Monte Carlo collision operators having physics of bound electrons and partially-ionized impurities to calculate the post thermal quench spatial distribution of REs. Ref.[25] uses a RE orbit module in MARS-F to calculate RE loss by magnetohydrodynamic (MHD) instabilities. The confinement of REs in stochastic magnetic fields characteristic of the thermal quench phase was studied in Ref. [26].

Additional previous studies have developed tools for modeling the transport of injected impurities. Ref. [27] developed KPRAD to study the effect of MGI on disruptions. Ref. [28] developed the 1D radial fluid code IMAGINE to model MGI with comparisons to JET interferometer diagnostics. Ref. [29] recently developed a 1D diffusion model for impurity profiles and evolution.

The present study builds on previous research by incor-

* corresponding author: beidlermt@ornl.gov

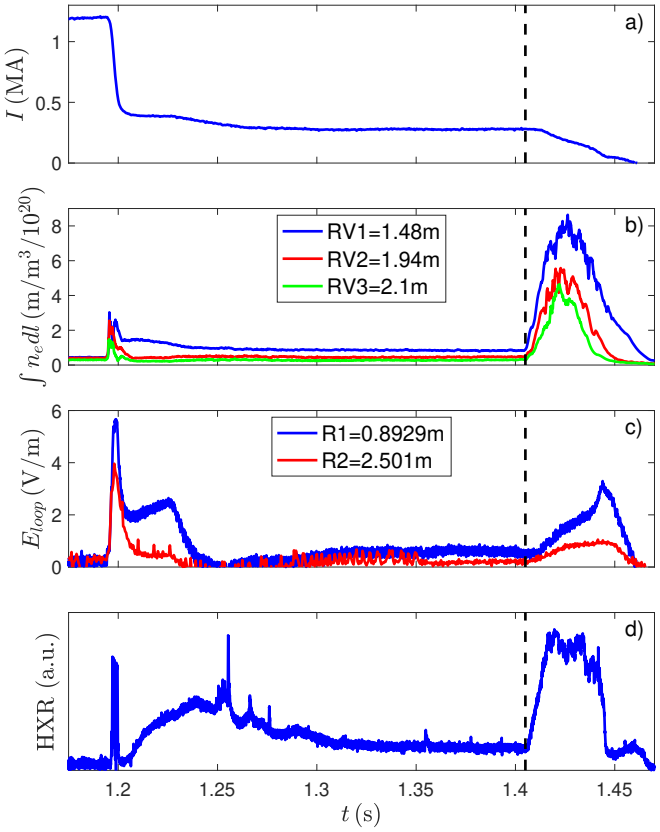

FIG. 1. DIII-D experiment #164409 with Ne MGI into the post-disruption, RE plateau, dissipating the RE current in panel a). The impurity injection results in greatly increased densities at time 1.405 ms (marked by vertical, dashed line) as seen by interferometer chord data in b). Changes in RE current after Ne MGI drive a toroidal loop voltage consistent with a toroidal electric field in panel c). REs interacting with the companion plasma and limiters produce hard x-rays in panel d).

porating experimentally-reconstructed, time-dependent magnetic and electric fields and employing models for the spatial-dependence of the injected impurity and electron density. Additionally, the flexible KORC framework is used to simulate RE dissipation with different models for bound electrons and partially-ionized impurity physics. The code KORC has been extended to serve as a general framework for simulating RE physics, including validation and verification of the theoretical models needed to understand RE dissipation by impurity injection.

A major theme and contribution of the present paper is the assessment of the effectiveness of RE dissipation given the competing time scales of the RE loss of confinement (due to the displacement of the flux surfaces and the eventual loss of magnetic confinement) and RE energy dissipation. The remainder of this paper is organized as follows. In Sec. II we introduce the extensions to KORC permitting the study of RE dissipation by impurity injection, including relativistic guiding center equations of motion, incorporating experimentally-reconstructed magnetic and toroidal electric fields, models for a spatiotemporal density profile, Monte Carlo linearized, Coulomb collision operator with models of bound electron effects, and synchrotron and bremsstrahlung radiation models. In Sec. III we discuss the initialization of the RE distributions used in KORC simulations. In Sec. IV we present results of KORC simulations and comparisons to DIII-D experiment #164409. Lastly, in Sec. V we provide concluding remarks.

II. PHYSICS MODEL

A. Relativistic Guiding-Center Equations

To make modeling RE orbits for the duration of the RE dissipation phase numerically feasible, we employ the relativistic guiding center (RGC) model from Refs. [30, 31]. We implement the RGC model in the limit that the magnetic field is static, which yields the equations of motion

$$\frac{d\mathbf{X}}{dt} = \frac{1}{\mathbf{b}\cdot\mathbf{B}^*}\left(e\mathbf{E}\times\mathbf{b} + \frac{m\mu\mathbf{b}\times\nabla B + p_\parallel \mathbf{B}^*}{m\gamma_{\rm gc}}\right) \quad (1a)$$

$$\frac{dp_\parallel}{dt} = \frac{\mathbf{B}^*}{\mathbf{b}\cdot\mathbf{B}^*}\cdot\left(e\mathbf{E} - \frac{\mu\nabla B}{\gamma_{\rm gc}}\right), \quad (1b)$$

where $\mathbf{X}\in\mathbb{R}^3$ denotes the spatial location of the GC in cylindrical (R,ϕ,Z) coordinates and $p_\parallel\in\mathbb{R}$ denotes the component of the relativistic momentum along the magnetic field, $p_\parallel \equiv \gamma m(\mathbf{V}\cdot\mathbf{b}) = \gamma m V\cos\eta$, with $\mathbf{V} = d\mathbf{X}/dt$ the velocity of the GC, $\mathbf{b} = \mathbf{B}/B$ the unit magnetic field vector, η the pitch angle relative to $\mathbf{b}$, m the particle mass, e the particle charge, $\gamma = \left[1-(V/c)^2\right]^{-1/2}$, and the magnitude of a vector $\mathbf{A}$ given by $A = \sqrt{\mathbf{A}\cdot\mathbf{A}}$. The magnetic moment is defined as

$$\mu = \frac{|\mathbf{p} - p_\parallel\mathbf{b}|^2}{2mB} = \frac{p_\perp^2}{2mB}, \quad (2)$$

and is assumed constant in the absence of collisions and radiation, with $p_\perp = \gamma m V\sin\eta$. The "effective" magnetic field is defined as

$$\mathbf{B}^* = q\mathbf{B} + p_\parallel\nabla\times\mathbf{b}, \quad (3)$$

and the GC relativistic factor is defined as

$$\gamma_{\rm gc} = \sqrt{1 + \left(\frac{p_\parallel}{mc}\right)^2 + \frac{2\mu B}{mc^2}}. \quad (4)$$

The static magnetic field limit of the RGC equations can be shown to be valid for the present case by scaling the right-hand-side (RHS) velocity terms for the spatial location

$$\begin{aligned} e\mathbf{E}\times\mathbf{b} \;&::\; p_\parallel\frac{\partial\mathbf{b}}{\partial t}\times\mathbf{b} \;::\; \frac{\mu}{\gamma}\mathbf{b}\times\nabla B \;::\; \frac{p_\parallel\mathbf{B}^*}{m_e\gamma} \\ e \;&::\; \gamma m_e c \;::\; \gamma m_e c^2\eta^2 \;::\; ec \\ 10^{-19} \;&::\; 10^{-21} \;::\; 10^{-14} \;::\; 10^{-11}, \end{aligned} \quad (5)$$

where we assume a RE has kinetic energy of 10 MeV and pitch angle of 10°, electric field, magnetic field, and spatial length scale are of order unity, and Faraday's law is

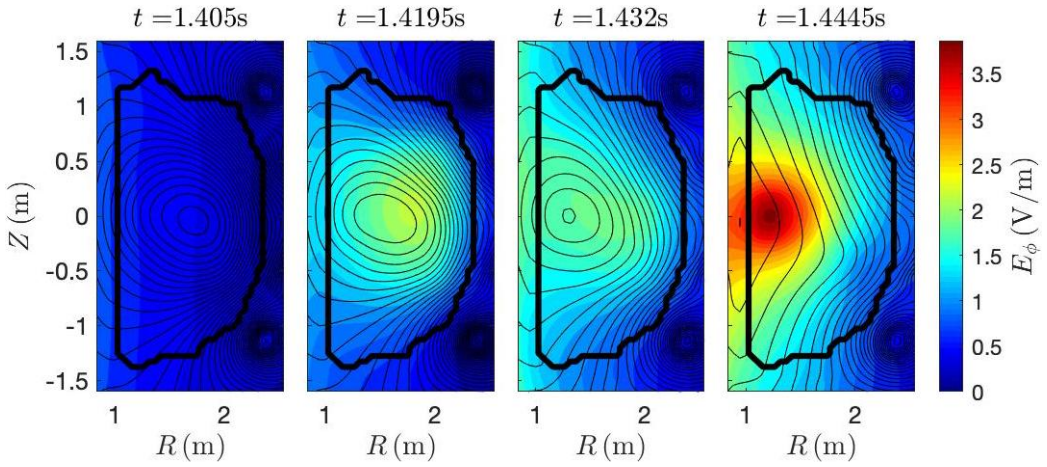

FIG. 2. Snapshots of the time-evolving, poloidal flux contours (thin, black contours) from DIII-D experiment #164409 as calculated with JFIT. The overlaid thick, black contour shows the approximate first wall of DIII-D. The colormap indicates the toroidal electric field as calculated from the time-derivative of the poloidal flux contours.

used to scale $\partial\mathbf{b}/\partial t$. The term coming from the covariant relativistic correction proportional to the time-derivative of the magnetic unit vector is the smallest contribution, and many orders of magnitude smaller than the leading terms. More precise calculations (not shown) also indicate the applicability of the static magnetic field limit used in the equations of motion in this work.

The model equations are integrated employing the Cash-Karp 5th order Runge-Kutta method [32]. For an axisymmetric magnetic configuration, in the absence of an electric-field, collisions, or radiation, energy and the canonical toroidal momentum are conserved. These conserved quantities are used as a way to test the accuracy of orbit calculations in a given magnetic configuration. We find that the accuracy of calculations are dependent on resolving the magnitude of magnetic curvature in the configuration, dominated by the motion parallel to the magnetic field, consistent with Eq. (5). Based on the results of a convergence study of time step (not shown), we use $dt = eB_0/\gamma m_e = 3.4321\times10^{-10}$ (s) in all simulations, calculated for a RE with kinetic energy of 10 MeV.

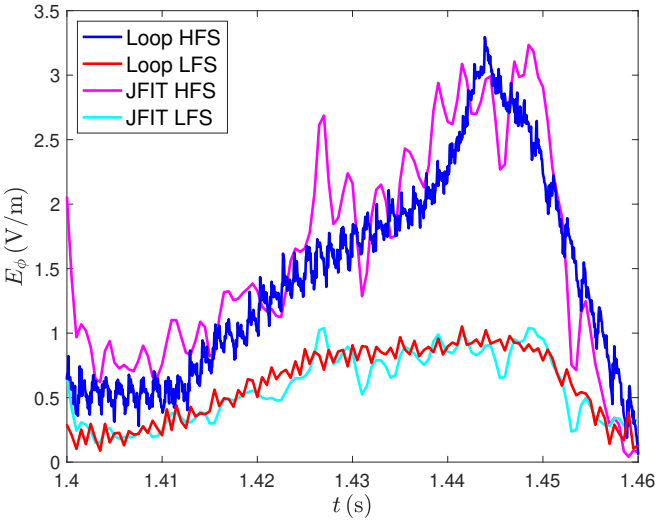

FIG. 3. Measurements of the toroidal electric field calculated via the toroidal loop voltage for DIII-D experiment #164409 at the HFS $R = 0.8929$ (m) (dark, blue trace) and the LFS $R = 2.5010$ (m) (red trace). Point measurements of the toroidal electric field calculated via time-derivatives of the JFIT poloidal flux function are shown at the HFS (violet trace) and LFS (cyan trace).

B. Plasma Model

The magnetic field components in the poloidal-plane are calculated from the poloidal flux function ψ_p as determined from JFIT reconstructions [33] of DIII-D discharges. The JFIT reconstruction differs from the more often used EFIT reconstruction [34], in that it doesn't find an Grad-Shafranov equilibrium, instead making a best fit to the available magnetic diagnostics. In the RE plateau, due to the low temperature and density of the companion plasma, the neutral beams needed for Motional Stark Effect [35] magnetic diagnostic are not available, due to the risk of shine through and damage to the first wall. Thus, there are no internal magnetic diagnostics available for constraining the JFIT equilibrium used in this study.

KORC uses JFIT-computed ψ_p on a $(NR \times NZ) = (33 \times 65)$ grid, which is then interpolated using the `PSPLINE` cubic spline interpolation routines [36]. In the cylindrical coordinate frame we adopt the convention $\mathbf{B}_p = \boldsymbol{\nabla}\phi \times \boldsymbol{\nabla}\psi_p$ for the poloidal field components yielding $B_R = (1/R)\partial\psi_p/\partial Z$, $B_Z = -(1/R)\partial\psi_p/\partial R$, where the gradients are computed using the spline representation in `PSPLINE`. In the discharges of interest the current is directed in the positive ϕ direction, giving ψ_p a local minimum at the magnetic axis. The toroidal magnetic field component is calculated assuming $B_\phi = -R_0B_0/R$, directed in the counter-I_p direction, where $R_0 = 1.682$ are the major radial locations of the geometric axis and $B_0 = 2.141$ are the magnitudes of the toroidal field at the geometric axis for DIII-D experiment #164409. In addition to calculating the magnetic field components by

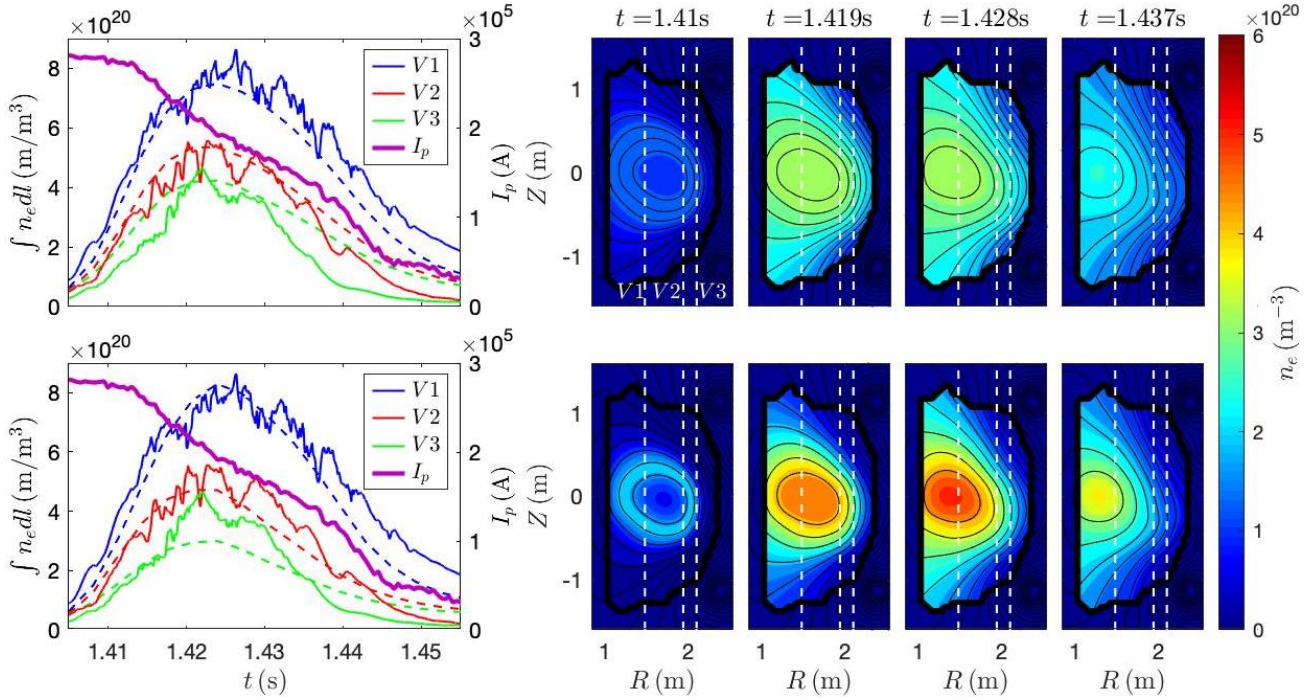

FIG. 4. Left plots show experimental current and line integrated density measurements in solid traces for DIII-D experiment #164409. Dashed traces indicate synthetic interferometer diagnostics, where the top plot uses a broad and diffuse spatiotemporal density profile with parameters in the top row of Table I and the bottom plot uses a narrow and dense spatiotemporal density profile with parameters from the bottom row. Right plots show spatiotemporal density profiles at different time slices, where the vertical dashed lines indicate the location of the interferometer diagnostics on DIII-D. Note that the different spatiotemporal profiles record similar synthetic interferometer signals.

$n_r\,(\mathrm{m}^{-3})$	$n_0\,(\mathrm{m}^{-3})$	$\tau_{\mathrm{in}}\,(\mathrm{s})$	$\tau_{\mathrm{out}}\,(\mathrm{s})$	$t_{\mathrm{delay}}\,(\mathrm{s})$	$\psi_{p,0}$	λ_n	$\tau_n\,(\mathrm{s})$
4×10^{20}	2.5×10^{19}	7.5×10^{-3}	1.25×10^{-2}	4×10^{-2}	0.8	0.255	1.5×10^{-2}
7×10^{20}	2.5×10^{19}	10^{-2}	1.25×10^{-2}	5×10^{-2}	0.775	0.15	1.75×10^{-2}

TABLE I. Spatiotemporal density profile fitting parameters for modeling DIII-D experiment #164409. Top row corresponds the a broad and diffuse profile while the bottom row corresponds to a narrow and dense profile.

taking the first derivatives using the `PSPLINE` routines, we also calculate the second order derivatives from the spline representation of ψ_p to compute the $\boldsymbol{\nabla} B$ and $\boldsymbol{\nabla}\times\mathbf{b}$ "auxiliary" fields needed to integrate Eqs. (1a-1b).

In this work, we use time-sequenced JFIT reconstructions of ψ_p that are spaced 0.5 ms apart. We preprocess this data with `MATLAB`, first smoothing ψ_p over 5 ms intervals, and then taking the time-derivative using a central difference method to calculate E_ϕ according to $E_\phi = (1/2\pi R)\partial\psi_p/\partial t$. Snapshots of the smoothed ψ_p contours are shown in Fig. 2, by the thin contours, where the thick contour indicates the DIII-D first wall. The calculated toroidal electric field is shown in Fig. 2 by the colormap. To check the robustness of the method for calculating E_ϕ, we compare values calculated from the JFIT reconstructions with data from loop voltages measurements from the HFS and LFS of DIII-D in Fig. 3. At the beginning of each simulation and 5 ms intervals thereafter, `PSPLINE` recalculates the interpolants for ψ_p and E_ϕ for the next time interval.

The electron temperature of the plasma is assumed temporally and spatially constant at $T_e = 1.5\,\mathrm{eV}$ as seen from Thomson scattering measurements taken before impurity injection (not shown). The effective impurity nuclear charge is also assumed temporally and spatially constant at $Z_{\mathrm{eff}} = 1$. The electron density takes the form of a temporally and spatially evolving, constricting "ring" profile. This profile is given by that of a Gaussian centered at a chosen flux surface with a time-dependent magnitude and width parameterized as

$$n_e(\psi_p,t) = \frac{n_r - n_0}{2}\left[\tanh\left(\frac{t-\tau_{\mathrm{in}}}{\tau_{\mathrm{in}}}\right) - \tanh\left(\frac{t-t_{\mathrm{delay}}}{\tau_{out}}\right)\right] \times \exp\left[-\frac{\left(\sqrt{\psi_p}-\sqrt{\psi_{p,0}}\right)^2}{2\sigma^2_{\psi_p}(t)}\right] \tag{6a}$$

$$\sigma_{\psi_p}(t) = \lambda_n\,\mathrm{erf}\left(\frac{t}{\tau_{\mathrm{n}}}\right) \tag{6b}$$

where n_r is the maximum density of the profile, n_0 is the background density, τ_{in}, τ_{out}, and t_{delay} parameterize the time scale over which the density increases, decreases, and remains constant, respectively, $\psi_{p,0}$ the poloidal flux surface where the Gaussian is centered, λ_n is the maximum width of the Gaussian, and τ_n is the time scale over which the Gaussian width increases. Roughly speaking, this analytic model implicitly contains the physics

of ionization, recombination, diffusion, and confinement to model the transport of electron and partially-ionized impurities. In the following simulations, two spatiotemporal profiles are used, a broad and diffuse profile, seen in the top row of plots in Fig. 4 with parameters in the top row of Table I, and a narrow and dense profile seen in the bottom row of plots in Fig. 4 with parameters in the bottom row of Table I. The left column of plots in Fig. 4 compare line-integrated electron density interferometer diagnostic data from DIII-D experiment #164409 with synthetic line-integrated density diagnostic applied to the model density shown in the right plots of Fig. 4. The two spatiotemporal density profiles were chosen to attempt to "bookend" the possible density profiles given the line-integrated measurements.

This work assume that all impurity charge states considered have the same spatiotemporal profile as n_e, with only changes their ratio n_j/n_e to be discussed in Sec. II C 3. Physically, as impurities are injected via SPI, they first encounter a post-TQ, cold plasma, with little ionization. As the impurities reach the RE beam, the impurities are rapidly ionized and they and the resulting electrons move along poloidal flux surfaces. This ring structure can be seen experimentally by visible cameras (not shown). Due to the low temperatures of the companion plasma, the electrons and impurities diffuse across magnetic surfaces [37]. Lastly, as the current decreases, the electrons and impurities are deconfined.

C. Coulomb Collisions

1. Monte Carlo Operator

In flux-conserving form, the Fokker-Planck partial differential equation (PDE) with a linearized Coulomb collision operator in azimuthally-symmetric spherical momentum space (*e.g.* [38])

$$\begin{aligned}\mathcal{C}(f) =&\frac{1}{p^2}\frac{\partial}{\partial p}\left[p^2\left(C_A\frac{\partial f}{\partial p}+C_F f\right)\right]\\ &+\frac{C_B}{p^2}\left[\frac{1}{\sin\eta}\frac{\partial}{\partial\eta}\left(\sin\eta\frac{\partial f}{\partial\eta}\right)\right]\end{aligned} \tag{7}$$

can be written [39] as two equivalent stochastic differential equations (SDEs) for the phase-space momentum, given by

$$\begin{aligned}dp =&\left\{-C_F(p)+\frac{1}{p^2}\frac{\partial}{\partial p}\left[p^2C_A(p)\right]\right\}dt\\ &+\sqrt{2C_A(p)}\,dW_p,\end{aligned} \tag{8a}$$

$$d\eta = \frac{C_B(p)}{p^2}\cot\eta dt+\frac{\sqrt{2C_B(p)}}{p}\,dW_\eta, \tag{8b}$$

where C_F, C_A, and C_B are transport coefficients for collisional friction (slowing down), parallel diffusion, and pitch angle scattering (deflection), respectively, and dW is a zero mean, unit standard deviation Weiner process satisfying

$$< dW >= 0, \qquad < (dW)^2 >= dt. \tag{9}$$

Here, we use uniformly-distributed random numbers, which behave better than normally-distributed random numbers at low energies, due to their tighter bounds. Applying Itô's lemma by letting $\xi = \cos\eta$ yields

$$d\xi = -2\xi\frac{C_B(p)}{p^2}dt-\frac{\sqrt{2C_B(p)}}{p}\sqrt{1-\xi^2}\,dW_\xi. \tag{10}$$

The Coulomb collision operator SDEs are subcycled independently of the RGC equations of motion using an operator splitting method. The time step of the collision operator is set as the 1/20 of the shortest inverse collision frequency (to be defined in the following subsections). While this temporal resolution accurately captures the damping of relativistic particles, with relatively long inverse collision frequencies, once particles thermalize this temporal resolution is not sufficient, consistent with the divergence of $d\eta$ as $p\to 0$. Thus, for this study, when a particle's momentum satisfies $p < m_e c$, the particle is flagged as thermalized and is not tracked anymore. Future studies, especially for the generation of runaways from a thermal plasma following the thermal quench, will require a significant increase in the collision substep cadence.

2. Relativistic Transport Coefficients

In the absence of bound electron and partially-ionized impurity physics, Ref. [18] generalizes the collision operator coefficients C_A, C_F, C_B to combine the nonrelativistic [38] and relativistic [40] energy limits, yielding

$$C_A(v) = \frac{\Gamma_{ee}\mathcal{G}(\frac{v}{v_{\rm th}})}{v}, \tag{11a}$$

$$C_F(v) = \frac{\Gamma_{ee}\mathcal{G}(\frac{v}{v_{\rm th}})}{T_e}, \tag{11b}$$

$$\begin{aligned}C_B(v) =& \frac{\Gamma_{ei}}{2v}Z_{\rm eff}+\frac{\Gamma_{ee}}{2v}\left[\mathrm{erf}\left(\frac{v}{v_{\rm th}}\right)\right.\\ &\left.-\mathcal{G}\left(\frac{v}{v_{\rm th}}\right)+\frac{1}{2}\left(\frac{v_{\rm th}v}{c^2}\right)^2\right],\end{aligned} \tag{11c}$$

where $\Gamma_{ee,ei} = n_e e^4\ln\Lambda_{ee,ei}/4\pi\epsilon_0^2$ with $\ln\Lambda_{ee,ei}$ the Coulomb logarithm for e-e(e-i) collisions, $v_{\rm th} = \sqrt{2T_e/m_e}$ the thermal electron velocity,

$$\mathcal{G}(x) = \frac{\mathrm{erf}(x)-x\,\mathrm{erf}'(x)}{2x^2} \tag{12}$$

is the Chandrasekhar function, where the prime indicates a derivative with respect to the independent variable. The expressions for $\ln\Lambda_{ee,ei}$ are taken from Ref. [7]

$$\ln\Lambda_{ee} = \ln\Lambda_0+\frac{1}{5}\ln\left\{1+\left[2(\gamma-1)c^2/v_{\rm th}^2\right]^{5/2}\right\} \tag{13a}$$

$$\ln\Lambda_{ei} = \ln\Lambda_0+\frac{1}{5}\ln\left[1+(2\gamma v/v_{\rm th})^5\right] \tag{13b}$$

$$\ln\Lambda_0 = 14.9-\frac{\ln n_e(10^{20}\,\mathrm{m}^{-3})}{2}+\ln T(\mathrm{keV}). \tag{13c}$$

Note that the term in Eq. (11c) proportional to $Z_{\rm eff}$ is taken from relativistic collision theory, and this term diverges as $v \to 0$. Using the relation $dp = m_e\gamma^3 dv$, the second term in the brackets of Eq. (8a) can be evaluated as

$$\frac{1}{p^2}\frac{\partial}{\partial p}\left[p^2 C_A(p)\right] = \frac{\Gamma}{\gamma^3 m_e v^2}\left\{\left[2\gamma^2\left(\frac{v}{c}\right)^2 - 1\right]\mathcal{G}\left(\frac{v}{v_{\rm th}}\right) + \frac{v}{v_{\rm th}}\,{\rm erf}'\left(\frac{v}{v_{\rm th}}\right)\right\}. \tag{14}$$

Note, that this form does not treat the momentum dependence in the Coulomb logarithm.

3. Bound Electrons

The transport coefficients given in Eqs. (11a-11c) describe normalized collision frequencies due to Coulomb collisions with ions and free electrons according to

$$C_A(v) \equiv \frac{p^2}{2}\nu_\parallel^{ee}, \tag{15a}$$

$$C_F(v) \equiv p\nu_S^{ee}, \tag{15b}$$

$$C_B(v) \equiv \frac{p^2}{2}\left(\nu_D^{ei} + \nu_D^{ee}\right), \tag{15c}$$

where the factor of 1/2 used in Ref. [38] for the definition Eq. (15b) has been absorbed into ν_S^{ee} as done in Ref. [7]. However the bound electrons of the partially ionized impurities will also play an important role. Reference [7] considers the effects of bound electrons on the slowing down e-e collision frequency by including a multiplicative factor

$$\nu_S^{ee} = \nu_{S,CS}^{ee}\left\{1 + \sum_j \frac{n_j}{n_e}\frac{Z_j - Z_{0j}}{\ln\Lambda}\left[\frac{1}{5}\ln(1+h_j^5) - \beta^2\right]\right\}, \tag{16}$$

where $\nu_{S,CS}^{ee}$ is the "completely screened" slowing down frequency consistent with the models neglecting bound electron physics given by Eqns. (15b,11b), the sum is over the ionization state, n_j is the density of the j-th ionization state, Z_j is the unscreened (*i.e.* fully ionized) impurity ion charge, Z_{0j} is the screened (*i.e.* partially ionized) impurity ion charge, $h_j = p\sqrt{\gamma - 1}/I_j$, where I_j is the mean excitation energy provided in Ref. [41], and $\beta = v/c$ is the usual relativistic speed. The factor $Z_j - Z_{0j}$ is recognized as the number of bound electrons a partially-ionized impurity charge state possesses. The following simulations assume that all impurity charge states considered have the same spatiotemporal profile as n_e, with only changes their ratio n_j/n_e satisfying

$$n_e = \sum_j k_j \times n_{j^{+k_j}}, \tag{17}$$

where k_j is the charge state for a particular partially-ionized impurity j. The effects of bound electrons on the pitch-angle diffusion e-i collision frequency is considered with the modification

$$\nu_{\rm D}^{ei} = \nu_{\rm D,CS}^{ei}\left(1 + \frac{1}{Z_{\rm eff}}\sum_j \frac{n_j}{n_e}\frac{g_j}{\ln\Lambda_{ei}}\right), \tag{18}$$

where $\nu_{D,CS}^{ei}$ is the completely screened pitch angle scattering frequency consistent with the models neglecting bound electron physics given by Eqn. (15c) and the first term of Eq. (11c),

$$g_j = \frac{2}{3}(Z_j^2 - Z_{0j}^2)\ln(y_j^{3/2}+1) - \frac{2}{3}\frac{(Z_j - Z_{0j})^2 y_j^{3/2}}{y_j^{3/2}+1} \tag{19}$$

with $y_j = p\bar{a}_j$, and $\bar{a}_j$ is the normalized effective ion scale length for impurity charge state j. The values $\bar{a}_j$ are determined from the density of bound electrons as calculated in Ref. [8]. Thus, with the Hesslow model of bound electrons and partially-ionized impurities, the transport coefficients become

$$C_{A,H}(v) = \frac{\Gamma_{ee}\mathcal{G}(\frac{v}{v_{\rm th}})}{v}, \tag{20a}$$

$$C_{F,H}(v) = \frac{\Gamma_{ee}\mathcal{G}(\frac{v}{v_{\rm th}})}{T_e}\left\{1 + \sum_j \frac{n_j}{n_e}\frac{Z_j - Z_{0j}}{\ln\Lambda_{ee}} \times \left[\frac{1}{5}\ln(1+h_j^5) - \beta^2\right]\right\}, \tag{20b}$$

$$C_{B,H}(v) = \frac{\Gamma_{ei}}{2v}Z_{\rm eff}\left(1 + \frac{1}{Z_{\rm eff}}\sum_j \frac{n_j}{n_e}\frac{g_j}{\ln\Lambda_{ei}}\right) + \frac{\Gamma_{ee}}{2v}\left[{\rm erf}\left(\frac{v}{v_{\rm th}}\right) - \mathcal{G}\left(\frac{v}{v_{\rm th}}\right) + \frac{1}{2}\left(\frac{v_{\rm th}v}{c^2}\right)^2\right]. \tag{20c}$$

Reference [7] also pointed to comments in Ref. [42] about the inclusion of bound electrons in avalanche phenomena. Reference [7] incorporated these comments by modifying the slowing down e-e collision frequency to include half of the bound electrons

$$\nu_S^{ee} = \nu_{S,CS}^{ee}\left(1 + \sum_j \frac{n_j}{n_e}\frac{Z_j - Z_{0j}}{2}\right). \tag{21}$$

We have also incorporated similar modifications to the pitch-angle diffusion e-i collision frequency

$$\nu_D^{ei} = \nu_{D,CS}^{ei}\left(1 + \sum_j \frac{n_j}{n_e}\frac{Z_j - Z_{0j}}{2}\right). \tag{22}$$

Thus, with the Rosenbluth-Putvinski model of bound electrons and partially-ionized impurities, the transport

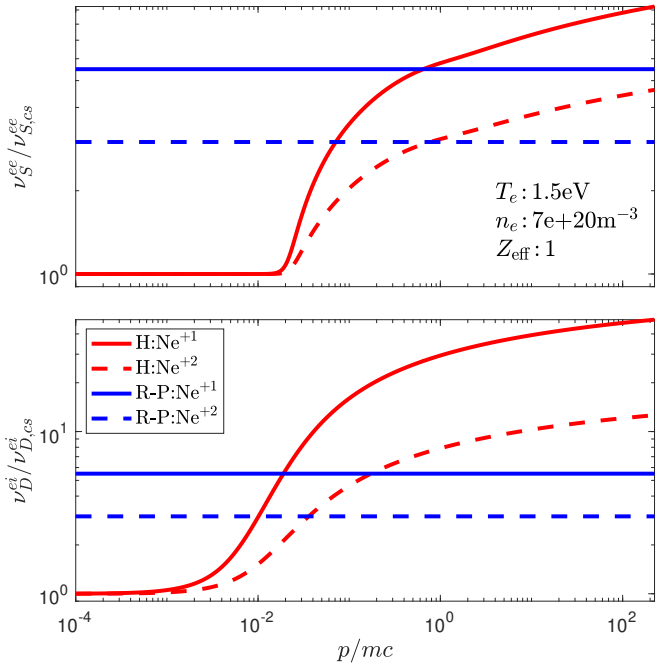

FIG. 5. Top plot shows the slowing down collision frequency with the inclusion of bound electrons normalized to the frequency without bound electron physics. Bottom plot shows the pitch angle diffusion collision frequency with the inclusion of bound electrons normalized to the frequency without bound electron physics. Red traces indicate the Hesslow model and blue traces indicate the Rosenbluth-Putvinski model. Solid traces are for Ne^{+1} and dashed traces for for Ne^{+2}.

coefficients become

$$C_{A,RP}(v) = \frac{\Gamma_{ee}\mathcal{G}(\frac{v}{v_{\rm th}})}{v}, \tag{23a}$$

$$C_{F,RP}(v) = \frac{\Gamma_{ee}\mathcal{G}(\frac{v}{v_{\rm th}})}{T_e}\left(1+\sum_j \frac{n_j}{n_e}\frac{Z_j - Z_{0j}}{2}\right), \tag{23b}$$

$$C_{B,RP}(v) = \frac{\Gamma_{ei}}{2v}Z_{\rm eff}\left(1+\sum_j \frac{n_j}{n_e}\frac{Z_j - Z_{0j}}{2}\right) + \frac{\Gamma_{ee}}{2v}\left[\mathrm{erf}\left(\frac{v}{v_{\rm th}}\right) - \mathcal{G}\left(\frac{v}{v_{\rm th}}\right) + \frac{1}{2}\left(\frac{v_{\rm th}v}{c^2}\right)^2\right]. \tag{23c}$$

In the following simulations, we will refer to 3 collision models, "No Bound" with transport coefficients given by Eqs. (11a-11c) with no bound electrons, "Hesslow" with transport coefficients given by Eqs. (20a-20c), and "R-P" with transport coefficient given by Eqs. (23a-23c). Figure 5 shows the slowing down frequency in the top plot and the pitch angle scattering frequency in the bottom plot for singly-ionized Ar and Ne using the Hesslow and R-P models. The collision frequencies are normalized to the completely screened, or No Bound, collision frequencies.

D. Radiation Damping

Simulations also include the effects of synchrotron radiation due to the radiation reaction force $\mathbf{F}_R$. The Landau-Lifshitz representation [43] of the Lorentz-Abraham-Dirac radiation reaction force, ignoring the electric field and advective derivatives, is

$$\mathbf{F}_R = \frac{1}{\gamma\tau_R}\left[(\mathbf{p}\times\mathbf{b})\times\mathbf{b} - \frac{1}{(m_e c)^2}(\mathbf{p}\times\mathbf{b})^2\,\mathbf{p}\right], \tag{24}$$

where $\tau_R = 6\pi\epsilon_0(m_e c)^3/(e^4B^2)$ is the radiation damping time scale. In azimuthally-symmetric spherical momentum space, with the identity $(\hat{p}\times\mathbf{b})\times\mathbf{b} = -\sin\eta\hat{p} - \cos\eta\hat{\eta}$, the flux-conserving form of the Fokker-Planck PDE can be written as two equivalent SDEs given by

$$\frac{dp}{dt} = -\frac{\gamma p}{\tau_R}(1-\xi^2) \tag{25a}$$

$$\frac{d\xi}{dt} = \frac{\xi(1-\xi^2)}{\tau_R\gamma}. \tag{25b}$$

Equation (25a) is consistent with the relativistic Larmor formula (*e.g.* [44]).

The evolution equations for (p,ξ) can be transformed into evolution equations for $(p_\parallel,\mu)$ yielding

$$\frac{dp_\parallel}{dt} = -\frac{p_\parallel(1-\xi^2)}{\tau_R}\left(\gamma - \frac{1}{\gamma}\right) \tag{26a}$$

$$\frac{d\mu}{dt} = -\frac{2\mu}{\tau_R}\left[\gamma(1-\xi^2) + \frac{\xi^2}{\gamma}\right]. \tag{26b}$$

These deterministic evolution equations are added to the Cash-Karp algorithm for integrating the GC equations of motion. We note that Eq. (24) is to be taken at the location of a moving charge, so the above implementation is only valid for a small gyroradius. A specific formulation for the GC equations of motion is given by Ref. [45] and will be explored in future studies.

The bremsstrahlung radiation due to runaway electrons interacting with impurities is discussed in Ref. [46] and can be written as

$$\frac{d}{dt}\left[(\gamma-1)m_e c^2\right] = -2vn_j\kappa Z_{0j}(Z_{0j}+1) \times \frac{\alpha}{\pi}(\gamma-1)\left[\ln(2\gamma) - \frac{1}{3}\right], \tag{27}$$

where $\kappa = 2\pi r_e^2 m_e c^2$, $r_e = e^2/4\pi\epsilon_0 m_e c^2$ is the classical electron radius, and $\alpha = 1/137$ is the fine structure constant. Because only the energy changes, and not the pitch angle, using $d\gamma/dp = v/(m_e c^2)$ we can write

$$\frac{dp}{dt} = -2n_j\kappa Z_{0j}(Z_{0j}+1) \times \frac{\alpha}{\pi}(\gamma-1)\left[\ln(2\gamma) - \frac{1}{3}\right] \tag{28}$$

$$\frac{d\xi}{dt} = 0. \tag{29}$$

Similarly as for synchrotron radiation, the evolution equations for (p,ξ) can be transformed into evolution

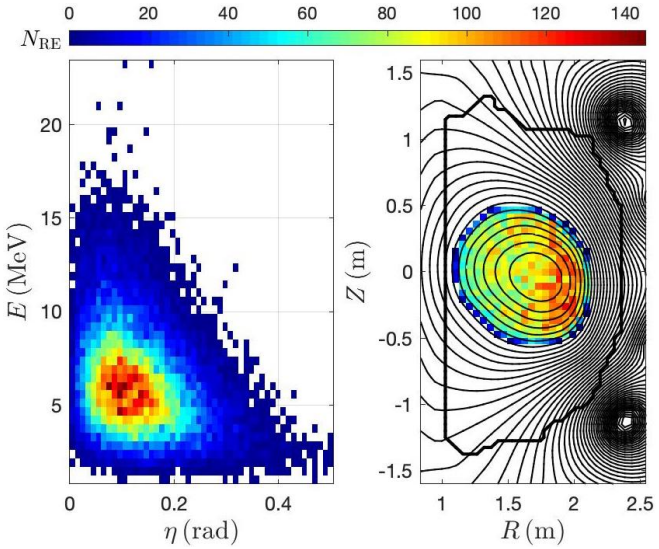

FIG. 6. Example initial distribution used for simulations of DIII-D experiment #164409 with Ne MGI with 2.5×10^4 sampled particles. E,η distribution shown in a), and R,Z distribution shown in b), with overlaid (thin) contours of ψ_p and (thick) first wall.

equations for $(p_\parallel,\mu)$ yielding

$$\frac{dp_\parallel}{dt} = -\xi 2n_j\kappa Z_{0j}(Z_{0j}+1) \times\frac{\alpha}{\pi}(\gamma-1)\left[\ln(2\gamma)-\frac{1}{3}\right] \tag{30}$$

$$\frac{d\mu}{dt} = -\frac{(1-\xi^2)p}{m_eB}2n_j\kappa Z_{0j}(Z_{0j}+1) \times\frac{\alpha}{\pi}(\gamma-1)\left[\ln(2\gamma)-\frac{1}{3}\right]. \tag{31}$$

III. ENSEMBLE INITIALIZATION

A Metropolis-Hastings (MH) algorithm [47, 48] is employed to sample user-provided distribution functions, sampling in multidimensional spatial-momentum phase space using a Markov-chains of Gaussian processes for each dimension. The "acceptance ratio" is calculated for every sample of the Markov-chains, comparing the new sample to the previous sample. If this ratio is greater than 1 or a uniformly-distributed random number, the new sample is accepted. Included in the acceptance ratio is the Jacobian determinant of the cylindrical spatial coordinate system R and the of the spherical momentum phase space $p^2\sin\eta$ at either sample. One benefit of the MH algorithm is that it only depends on the ratio of the distribution function at different sampling points, and not the absolute values, thus no normalizations are needed.

For the following simulations, we use an initial distribution of the form

$$f[\psi_p(R,Z),\mathcal{E},\eta] = f_{\psi_p}[\psi_p(R,Z)]f_{\mathcal{E}}(\mathcal{E})f_\eta(R,\mathcal{E},\eta), \tag{32}$$

where $\mathcal{E}=\gamma m_ec^2$ is the total energy of a RE. Across all

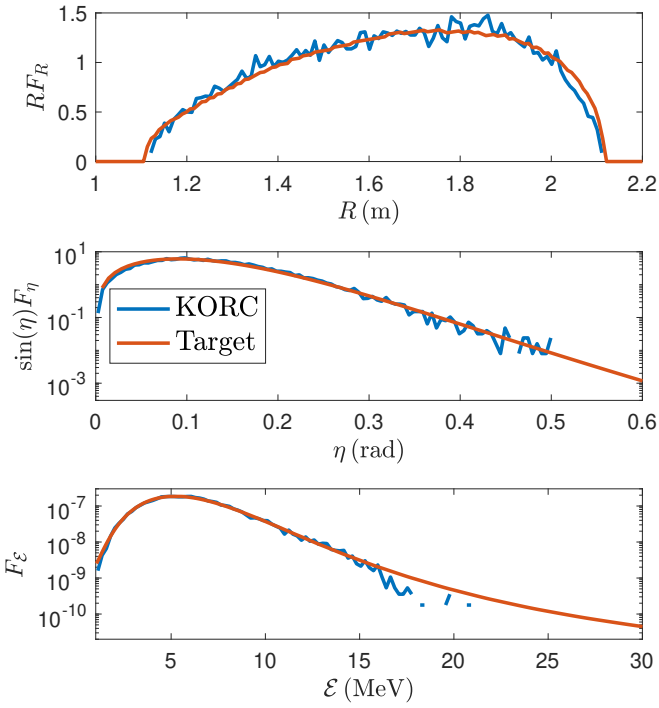

FIG. 7. Comparison between the target distribution (red traces) compared to the sampled distribution (blue traces) for a given KORC calculation. The top plot shows the spatial distribution for a uniform density of REs distributed along the poloidal flux surfaces for DIII-D experiment #164409. The middle plot shows the pitch angle distribution given by Eqs. 34,35. The bottom plot shows the energy distribution for sampling of the distribution function inferred from a separate DIII-D experiment reported in Ref. [49].

simulations to be presented, we assume that the initial spatial distribution only depends on ψ_p as a Gaussian

$$f_{\psi_p}(R,Z) = \exp\left[-\frac{\psi_N(R,Z)}{\sigma_{\psi_N}}\right], \tag{33}$$

where $\psi_N=[\psi_p(R,Z)-\psi_{p,\mathrm{axis}}]/(\psi_{p,\mathrm{lim}}-\psi_{p,\mathrm{axis}})$ is the normalized poloidal flux, with $\psi_{p,\mathrm{axis}}=0.600\,\mathrm{Wb}$ is the poloidal flux at the magnetic axis and $\psi_{p,\mathrm{lim}}=0.845\,\mathrm{Wb}$ is the poloidal flux at the HFS limiter, $\sigma_{\psi_N}=10^6$ sets a uniform density, and an indicator function is used to limit sampling to where $\psi_N<0.845$. The particles are sampled uniformly in toroidal angle ϕ. For $f_{\mathcal{E}}(\mathcal{E})$ we use either a monoenergetic distribution of 10 MeV or the "Hollmann" distribution, inferred from experimental data of a post-disruption, RE beam in Ref. [49]. For the pitch angle distribution we use either a monopitch distribution of 10° or that considered in Ref. [49]

$$f_\eta(R,\mathcal{E},\eta) = \frac{A(R,\mathcal{E})}{2\sinh A(R,\mathcal{E})}e^{A(R,\mathcal{E})\xi}, \tag{34}$$

with

$$A(R,\mathcal{E}) = \frac{2E_\phi(R)}{Z_{\mathrm{eff}}+1}\frac{\gamma^2-1}{\gamma}, \tag{35}$$

where $E_\phi(R)=24.56E_{\mathrm{CH}}R_0/R$ is the approximate initial toroidal electric field, with the Connor-Hastie field [50]

$E_{\rm CH} = n_e e^3 \ln\Lambda_0/4\pi\epsilon_0^2 m_e c^2$, and $Z_{\rm eff} = 1$ is effective impurity nuclear charge.

For the nontrivial energy and pitch angle distribution from Ref. [49], the resulting distribution function is shown in Fig. 6 in a) E, η and b) R, Z phase space for 2.5×10^4 particles. Note that Fig. 6b) has overlaid (thin line) contours of ψ_p, consistent with the initial time in Sec. II B, and indicates the (thick line) approximate first wall on DIII-D. The apparent increase in the number of REs as R increases reflects the Jacobian determinant of the cylindrical coordinate system appearing when we integrate over the ϕ direction to show the distribution in the R, Z plane.

A comparison between the target distribution and sampled distribution is presented in Fig. 7. The top plot shows the distribution $F_R(R) = \int f_{\psi_p} dZ$, where the factor of R comes from the Jacobian determinant of the cylindrical coordinate system used for the spatial representation. The middle plot shows the distribution $F_\eta = \int dZ \int RdR \int d\mathcal{E} f$, where the factor of $\sin(\eta)$ comes from the Jacobian determinant of the spherical coordinate system used for the momentum representation. And lastly the bottom plot shows the distribution $F_\mathcal{E} = f_\mathcal{E}$ from Ref. [49]. Note that because the target $F_\mathcal{E}$ decreases algebraically, rather than exponentially, the Gaussian process MH algorithm has difficulties sampling the high energy tail. However, since the majority of the RE beam energy is contained in the bulk around 6.5 MeV, this sampling is acceptable for the present modeling.

IV. RESULTS

To characterize the evolution of the ensemble of particles at a macroscopic level, we define the total RE energy $\mathcal{E}_{\rm RE}$

$$\mathcal{E}_{\rm RE}(t) = m_e c^2 \sum_i^{N_p} \gamma_i(t) \mathcal{H}_{{\rm RE},i}(t) \tag{36}$$

where

$$\mathcal{H}_{{\rm RE},i}(t) = \begin{cases} 1 & \text{if } p_i(t) > m_e c \\ 0 & \text{if } p_i(t) < m_e c \text{ or hits wall.} \end{cases}$$

$\mathcal{H}_{\rm RE}$ effectively splits the ensemble of particles into two populations, confined and thermalized or deconfined electrons. Note that this definition is consistent with the discussion at the end of Sec. II C. We also define the RE current $I_{\rm RE}$, beginning from the toroidal current density $J_\phi = -en_e \mathbf{v}\cdot\hat{\phi}$, satisfying $I_{\rm RE} = \int dR \int dZ J_\phi$. Using the definition of the density of an ensemble of particles $n_e(\mathbf{x}) = \sum_i \delta^3(\mathbf{x}-\mathbf{x}_i) = \sum_i \delta(R-R_i)\delta(Z-Z_i)/(2\pi R)$ and assuming that the toroidal component of the velocity is, to lowest order, $\mathbf{v}\cdot\hat{\phi} \simeq v_\parallel \mathbf{b}\cdot\hat{\phi} = v\xi b_\phi$ yields

$$I_{\rm RE}(t) = -\frac{e}{2\pi} \sum_i^{N_p} \frac{v_i \xi_i b_{\phi,i}}{R_i} \mathcal{H}_{{\rm RE},i}(t). \tag{37}$$

To make comparisons between simulations and experiments, which contain vastly different total energy and current, we normalize these dissipating quantities to their initial values $\mathcal{E}_{\rm RE}(0)$ and $I_{\rm RE}(0)$. The initial values correspond to time 1.405 ms from DIII-D experiment #164409.

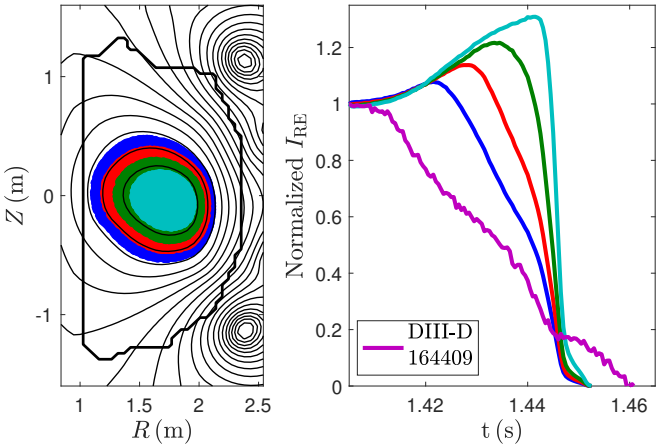

FIG. 8. Subsets of REs, delineated by initial value of poloidal flux function consistent with the left figure, to study the effect of different beam widths, made possible by the linear nature of individual RE orbits. Calculations performed with evolving magnetic configuration and consistent electric field, but without radiation or collisions.

The following calculations all use dynamic magnetic and electric fields unless otherwise noted, and synchrotron and bremsstrahlung radiation. We note that the role of radiation for the present study of RE dissipation by impurity injection, as compared to RE generation, are negligible (not shown). For simulations including collisions, the collision frequency is evaluated assuming the companion plasma contains two partially-ionized impurity charge states, with $n_{Ne^{+1}}/n_{Ne^{+2}} = 2$. This choice of impurity composition is roughly in line with results presented in Ref. [29]. With the impurity charge state ratio and electron density supplied, the impurity charge state densities are calculated with Eq. (17).

A. Confinement Losses

We begin by simulating a RE beam without any collisions, which decouples the effects of deconfinement of REs due to the evolution of the experimentally-reconstructed fields from collisional effects. Fig. 8 shows such a simulation, where we indicate different initial RE beam widths in the left plot, including particles within $\psi_N < 1.0$ in dark blue, $\psi_N < 0.78$ in red, $\psi_N < 0.56$ in green, and $\psi_N < 0.34$ in light blue. This is accomplished by a single simulation with a spatially uniform RE distribution, because of the linear nature of RE orbits. The right plot of Fig. 8 indicates that as the initial RE beam width gets smaller, the effect of deconfinement is delayed. Physicallyt, the smaller radii beams will not interact with the inner wall until later times, but then will have all their particles deconfined rapidly. The most extreme case would be a pencil beam, which would not lose any particles until the beam touches the wall, and

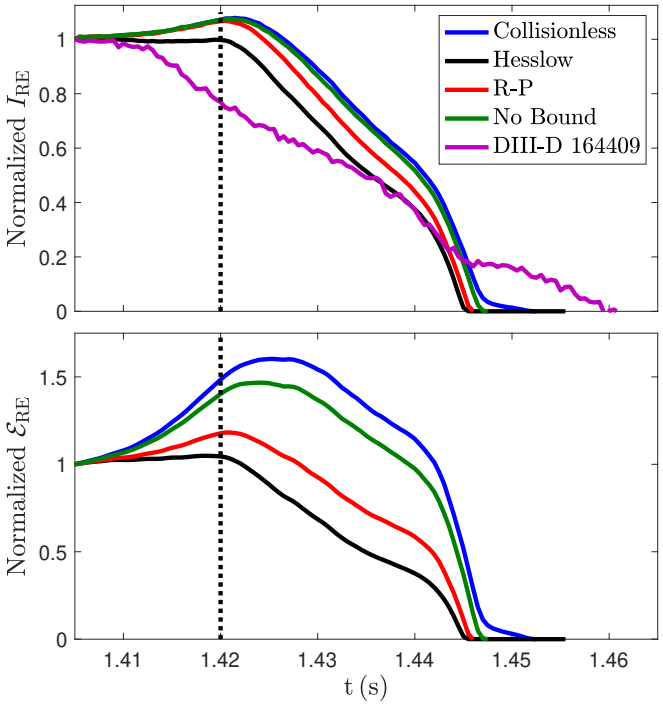

FIG. 9. Comparison of evolution of normalized RE beam current (top plot) and RE beam energy (bottom plot) for different bound electron models. Each calculation uses the consistent electric field for the evolving magnetic configuration and radiation. The black trace uses the Hesslow bound electron model, the blue trace uses the R-P model, the red trace uses no bound electrons, and the green trace does not include collisions. The vertical, dashed, black line indicated the approximate time that deconfinement begins to play a role, as estimated from Fig. 12.

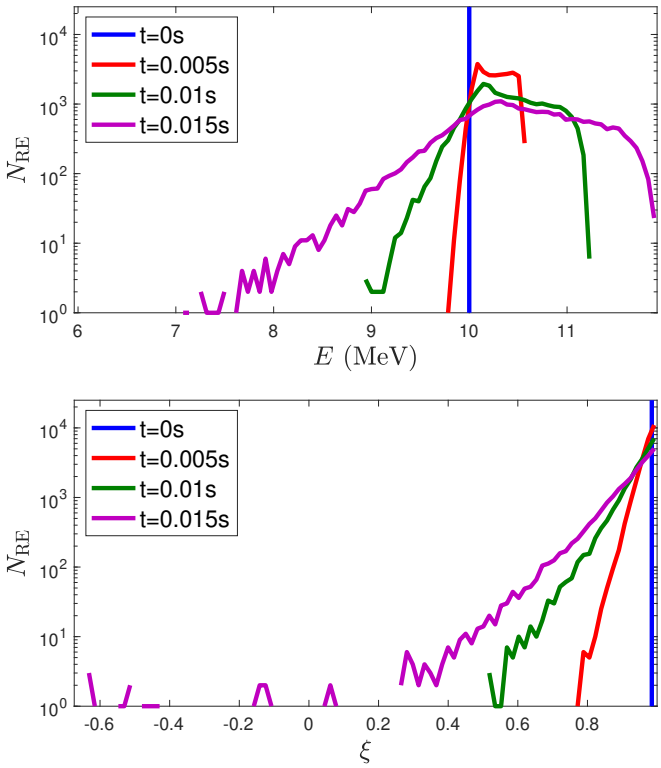

FIG. 10. Evolution of the RE ensemble energy (top plot) and cosine of the pitch angle (bottom plot) for the simulation in Fig. 9 using the Hesslow bound electron model. Traces show the distributions every 5 ms until confinement begins to degrade as estimated from Fig. 12.

then all particles would be lost nearly instantaneously. The normalized I_{RE} for each subset of simulated REs is compared to the experimental current from DIII-D experiment #164409, indicated by the violet trace.

The increase in normalized RE current is a surprising result. As the magnetic configuration evolves, the magnetic axis advects toward the HFS, decreasing the major radial location of REs summed in Eq. (37). This makes intuitive sense, as all REs are approximately traveling at c in the toroidal direction, starting at a pitch of $\eta = 10°$ with a small spread in pitch angle due to spatial orbit effects [11]. Without collisions, this speed remains the same, and as the RE beam advects toward the HFS, where the toroidal orbit length decreases linearly with R, there will be a higher charge per time through a specified toroidal angle. There will also be an additional effect due to pitch angle "pinching" due to the toroidal electric field, but we find that this is a small effect compared to the major radial location (not shown).

At the time after all REs are either deconfined or thermalized in this and each of the following simulations, DIII-D experiment #164409 shows current remaining for an additional 10 ms. With the present modeling capabilities of KORC, we are unable to study this directly, however we posit that it is due to the evolution of the companion plasma or secondary REs generated by large-angle collisions during this time period of larger induced toroidal electric field. We will discuss this further in Sec. V.

B. Bound electron modeling

We continue our study by including Coulomb collisions, and investigating the effect of different models of bound electron physics developed in Secs. II C 2 and II C 3. Figure 9 shows the dependence of the bound electron model on the normalized RE current (top plot) and energy evolution. The blue trace corresponds to the case without collisions shown as the dark blue trace in Fig. 8, the black trace uses the Hesslow bound electron model from Eqns. 20a-20c, the red trace uses the R-P bound electron model from Eqns. 23a-23c, the green trace uses the No Bound electron model from Eqns. 11a-11c, and the violet trace is the current from DIII-D experiment #164409. The vertical, dashed, black line indicated the approximate time that deconfinement begins to play a role, as estimated from Fig. 12. Progressing from no collisions to the No Bound, R-P, and lastly Hesslow collision models, the KORC simulated normalized RE current more closely aligns with the experimental current.

While nearly all the KORC simulations have their normalized RE current evolve qualitatively similarly, there is great disparity in how the normalized RE energy evolves in each case. Each model has the energy increasing until

after confinement is lost, with the main difference being the rate at which energy increases due to acceleration by the toroidal electric field in each case. The collisional slowing down is nonexistent in the no collisions simulation and is so weak in the No Bound model, that both cases still have energy increasing after loss of confinement. For these parameters, it is striking how the No Bound electron model is barely different from no collision case, pointing to the conclusion that the inclusion of a bound electron model is essential for recovering accurate simulation results. The simulating incorporating the Hesslow model is only one to have any current dissipate before loss of confinement, albeit at the small amount of $> 1\%$, and the least energy increase of 4.5% The simulation using the R-P bound electron model yields similar results to that using the Hesslow model, but due to greatly increased pitch angle scattering, by a factor of 7.15 at 10 MeV, and marginally increased collisional friction, by a factor of 1.33 at 10 MeV, in Hesslow model, as seen in Fig. 5.

To better understand how the RE ensemble averaged energy and current, it is instructive to directly view the evolution of the energy and pitch angle distributions. Figure 10 shows the evolution of the energy (top plot) and cosine of the pitch angle (bottom plot) for the simulation using the Hesslow bound electron model. Before REs begin to be deconfined, it is clear that the average energy is increasing, while ξ is decreasing, or rather η is increasing. We view ξ as compared to η, because ξ is a direct input into the calculation of the current consistent with Eq. (37). We posit that the energy is increasing due to REs being accelerated by the induced toroidal electric field more than decelerated by collisional slowing down. Comparing the approximate time rate of change of the momentum due to the induced toroidal field $dp/dt = -eE_\phi\xi$ and collisional slowing down for the initial RE energy and pitch, the electric force is initially equal to the collisional slowing down and increases as a larger toroidal electric field is induced. Conversely, we posit that the pitch angle is increasing due to collisional pitch angle scattering with the Hesslow bound electron model greater than the pinching effect due to the induced toroidal electric field. Comparing the time rate of change of the cosine of the pitch angle due to the induced toroidal field $d\xi/dt = -eE_\phi(1-\xi^2)/p$ and collisional pitch angle scattering for the initial RE energy and pitch, the collisional pitch angle scattering is approximately 10^2 larger than the electric force.

C. Parametric Modeling

Now that we have discussed the effects of deconfinement and bound electron models, we turn our attention to the parameterization of the initial RE distribution and spatiotemporal electron and partially-ionized impurity profile. Figure 11 shows the dependence of initial RE distribution and spatiotemporal density profile on the normalized RE current (top plot) and energy evolution (bottom plot). The dark blue trace corresponds to the case without collisions shown as the dark blue trace in Fig. 8, the dotte4d, dark blue trace corresponds to the case without collisions or the dynamic toroidal electric field, the black trace labeled as the canonical case uses the Hesslow bound electron model shown in Fig. 9, the red trace is the canonical case using the initial RE energy and pitch distribution from Ref. [49], the green trace is the canonical case using the narrow and dense spatiotemporal density profile, and the orange trace is the canonical case using both the initial RE energy and pitch distribution from Ref. [49] and the narrow and dense spatiotemporal density profile.

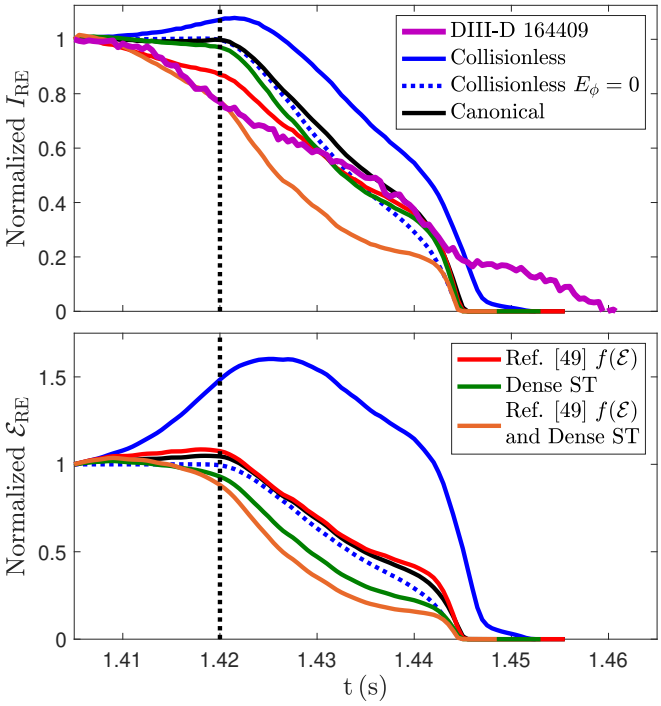

FIG. 11. Comparison of evolution of normalized RE beam current (top plot) and RE beam energy (bottom plot) for a hierarchy of models. All calculations use the electric field consistent with the evolving magnetic configuration and radiation unless otherwise noted. The black trace is the canonical case that includes collisions using the Hesslow bound electron model, the broad and diffuse spatiotemporal density profile, and an initial monoenergetic RE beam of 10 MeV. The dark blue trace does not include collisions, the dotted, dark blue trace does not include collisions or the dynamic toroidal electric field, the red trace uses the energy and pitch distribution form Ref. [49], the green trace uses the narrow and dense spatiotemporal density profile, the orange trace uses the energy and pitch distribution from Ref. [49] and the narrow and dense spatiotemporal density profile, and the violet trace is from DIII-D experiment #164409.

The collisionless simulation without the induced toroidal electric field indicates that the effect of the toroidal electric field nearly balances out collisional dissipation, as it is nearly identical to the canonical case. This reinforces our estimation of the comparison of the two forces from the end of Sec. IV B.

It can be seen that varying the initial energy and pitch distribution has a significant effect on current dissipation but not energy dissipation. We posit that this is due to lower initial mean energy, which yields a larger pitch

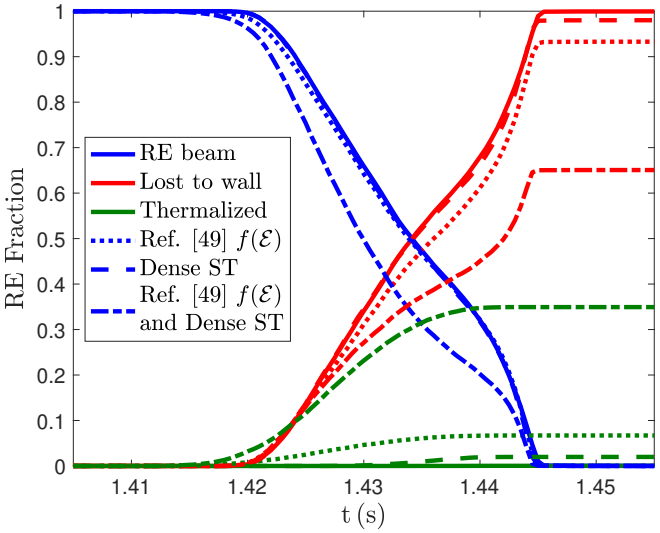

FIG. 12. Time evolution of the number of confined REs (blue traces), deconfined REs (red traces), and collisionally dissipated REs (green traces), where the solid traces correspond to the canonical simulation, the dotted traces correspond to the simulation using the initial energy and pitch distribution from Ref. [49], the dashed traces correspond to the simulation using the narrow and dense spatiotemporal density profile, and the dash-dotted traces correspond to the simulation using both the initial RE energy and pitch distribution from Ref. [49] and the narrow and dense spatiotemporal density profile.

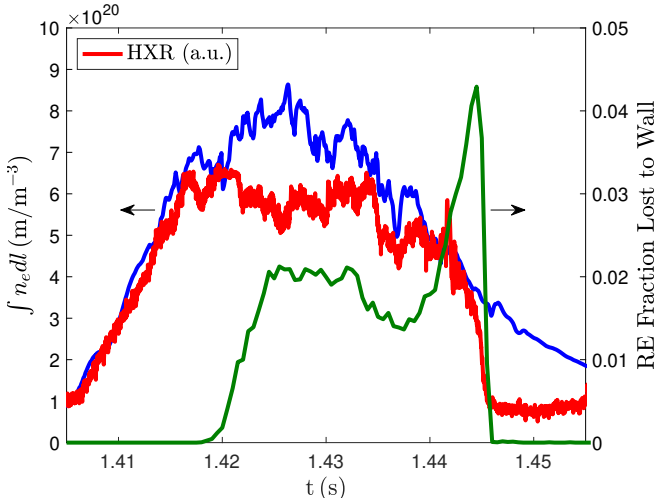

FIG. 13. Comparison between the V1 interferometer diagnostic (blue trace) and HXR signal (red trace) for DIII-D experiment #164409 with the RE fraction lost to the wall for the canonical KORC calculation (solid green trace).

angle scattering consistent with Eq. (8b) or (10) that varies as $1/p^2 \sim 1/E^2$.

Varying spatiotemporal density profile to use narrow and dense profile has a marginal effect on current dissipation but significant effect on energy dissipation. We posit that this is due to the collisional force being approximately twice as large as the toroidal electric force for the initial conditions for the more dense spatiotemporal density profile, whereas it was approximately equal for the more diffuse spatiotemporal density profile. By itself, varying the spatiotemporal density profile decreases the normalized energy before deconfinement, but only by 7%.

When the effects of the different initial energy and pitch distribution and denser spatiotemporal density are combined, both the current and energy are dissipated to a higher degree than either of the effects separately. This can be viewed as the best case scenario from the modeling of RE mitigation via Ne MGI in DIII-D experiment #164409. There is, however, a shortfall in the simulated current after confinement degrades for the case with combined effects. We posit that this shortfall would be augmented by the evolution of the companion plasma or secondary REs generated by large-angle collisions during this time period of larger induced toroidal electric field. As was the case in Sec. IV A, we will discuss this further in Sec. V.

We can also view the evolution of particles in the RE beam, deconfined particles impacting the wall, and thermalized particles whose momentum fall below $p < m_e c$. Figure 12 shows the evolution of particles in the RE beam (blue traces), deconfined particles (red traces), and thermalized particles (green traces) for simulations presented in Fig. 11, where the canonical simulation is indicated with solid traces, the simulation with initial RE energy and pitch distribution from Ref. [49] indicated by the dotted traces, the simulation with the more dense spatiotemporal density profile indicated by the dashed traces, and the simulation combining both effects by the dash-dotted traces.

The previous results are borne out clearly in Fig. 12, namely that the majority of REs across all simulations are lost to the wall, rather than thermalized. The canonical simulation is the most dire situation with $> 0.1\%$ thermalized, the dense ST simulation has 2% thermalized, the simulation with initial RE energy and pitch distribution from Ref. [49] has 7% thermalized, and the simulation with combined effects is again the best case scenario with 35% thermalized. The simulations using initial RE energy distribution from Ref. [49] have lower average initial distribution energy, where the collisional slowing down is more effective.

D. Additional Experimental Connections

In Fig. 1d, the HXR emission is observed to increase rapidly upon the injection of Ne gas into the post-disruption RE beam. The HXR signal (red trace) has been reproduced in Fig. 13, and plotted with the line integrated electron density from vertical chord V1 (blue trace) and the simulated RE fraction lost to the wall for the canonical KORC calculation (green trace). The HXR detector observes radiation emitted by REs when striking first wall or bulk ions and neutrals in plasma, thus both sources require REs for any signal. The initial rise in HXR correlates directly with the interferometer signal. There is also good agreement between the HXR signal the deconfinement of simulated REs. The final

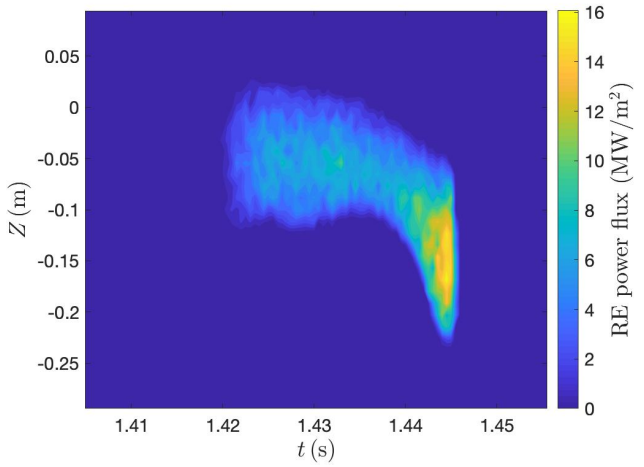

FIG. 14. Power flux on the inner wall calculated for the canonical KORC calculation. The total number of experimental REs was estimated and used to scale up the KORC calculated REs to arrive at a physically significant value. The axisymmetric magnetic field configuration leads to REs impacting the inner wall uniformly in the toroidal direction.

spike in RE fraction lost to the wall is not seen in the HXR signal. This indicates that future analysis is required to determine the proportionality constants to the total HXR signal coming from RE interaction with companion plasma and with wall separately. Lastly, because the HXR signal does not fully drop to the offset value, it indicates that there are additional REs remaining after KORC simulations expect all REs to be deconfined. This is further evidence that large-angle collisions are generating additional REs when the induced toroidal electric field is large near the end of the RE beam deconfinement, and will be discussed more in Sec. V.

Because KORC evolves the momentum and location of all simulated particles, it is possible to calculate the power flux to the wall when REs are deconfined. As there are of the order 10^{16} REs in a standard RE beam for DIII-D parameters, and only 2.5×10^4 REs simulated with KORC, it is necessary to calculate a scaling factor to calculate an experimental relevant power flux. We scale the initial current from DIII-D experiment #164409 $I_0 = 2.813\times10^5\,\mathrm{A}$, by that calculated using Eq. (37) $I_{\mathrm{RE}}(0) = 1.15\times10^{-7}$ to get a ratio of 2.45×10^{12}. In our calculations of the power flux, we assume every particle represents a physical number of particles equal to the calculated ratio. As the magnetic configuration is axisymmetric, so is the RE deposition on the inner wall (not shown). The power flux is calculated by binning in the Z direction in $[-0.3, 0.1]\,\mathrm{m}$, and summing up the particle energy deposited in a given bin per 0.5 ms. The calculation of the power flux varies as the spatial bin width is varied (not shown); the results presented in Fig. 14 are for 35 bins of width 1.1 cm. Future work will include comparing these deposition power fluxes to infrared camera images.

V. CONCLUSIONS AND DISCUSSION

Simulations performed with the kinetic RE code KORC incorporate experimentally-reconstructed, time-dependent magnetic and electric fields, and line integrated electron density data to construct spatiotemporal models of electron and partially-ionized impurity transport in the companion plasma. We use KORC to model DIII-D experiment #164409 that injects Ne MGI in order to mitigate a post-disruption, vertically-controlled, RE beam. Comparison of KORC results and experimental current evolution are performed including Coulomb collisions with different models of partially-ionized impurity physics, and it is found that the model presented in Ref. [7] most closely reproduce the experimental current evolution. Comparison of KORC results and experimental current evolution are performed for different models of initial RE energy and pitch angle distributions and different spatiotemporal electron and partially-ionized impurity transport. The majority of KORC calculations indicate that while the RE beam current is decreasing, the RE beam energy increases until confinement degrades. We posit that collisional pitch angle scattering is primarily responsible for decreasing the current, while the electric field accelerates REs more than collisional friction slows them down. The current decay lowers the rotational transform, which leads to deconfinement of REs. Using KORC results on the RE energy when striking the first wall, we make predictions of the power flux on the inner wall during RE deconfinement.

The contained results have immediate relevance for present fusion research, ITER, and future reactor level tokamaks. This work quantifies the efficacy of RE mitigation via injected impurities, and yields a relative importance of effects. The zeroth order effect is the dynamic magnetic field configuration that determines confinement of REs as summarized by Fig. 8 in Sec. IV A. First order effects are the inductive toroidal electric field as viewed in Fig. 11 of Sec. IV C, the partially-ionized impurity model as viewed in Fig. 9 of Sec. IV B, spatiotemporal density and partially-ionized impurity transport as viewed in Fig. 11 of Sec. IV C, and initial RE energy and pitch distribution as viewed in Fig. 11 of Sec. IV C. Synchrotron and bremsstrahlung radiation are much smaller effects for the dissipation process in DIII-D experiment #164409 and are not shown. A major contribution of the present study is the identification of the critical role played by loss of confinement in comparison with the relatively slow collisional damping.

This work is just the beginning of the necessary modeling effort of important effects still to be explored. Additional preliminary studies are underway of the spatiotemporal transport of injected impurities, separately looking at Ar injection, varying the amount of injected impurities, SPI injection technology, and injection into different tokamaks, such as JET and KSTAR. An important next development for KORC is the implementation of a large-angle collision operator. The magnetic to kinetic energy conversion by large-angle collisions upon the termination of the RE beam is an ongoing topic of research [14, 37, 51–53]. The injection of impurities provides additional elec-

trons to knock-on [54], and the induced toroidal electric field is greatest when magnetic configuration is rapidly deconfining. The large RE losses can induce a large toroidal electric field that may increase the Ohmic current, possibly explaining the results in Secs. IV A,IV C, and IV D. Because large-angle collisions produces REs at large pitch angles [55], these REs could potentially add a significant amount of energy to the RE beam without an associated increase in current. Lastly, tight coupling with an MHD code having impurity and ablation models is ultimately necessary for robust, predictive modeling of RE evolution. Such simulations will require calculation of the self-consistent, induced electric field as the RE ensemble evolves, and the resulting evolution of the magnetic configuration evolving with RE current and companion plasma.

ACKNOWLEDGMENTS

The first author would like to thank J. Herfindal, E. Hollmann, M. Lehnen, A. Lvovskiy, C. Paz-Soldan, and R. Sweeney for their insight into post-disruption, RE experiments, and M. Cianciosa, D. Green, J. Lore, H. Lu, and S. Seal for their help with improving KORC.

This material is based upon work supported by the U.S. Department of Energy, Office of Science, Office of Fusion Energy Sciences, using the DIII-D National Fusion Facility, a DOE Office of Science user facility, under Awards DE-FC02-04ER54698 and DE-AC05-00OR22725. This research also uses resources of the National Energy Research Scientific Computing Center (NERSC), a U.S. Department of Energy Office of Science User Facility operated under Contract No. DE-AC02-05CH11231.

This manuscript has been authored by UT-Battelle, LLC under Contract No. DE-AC05-00OR22725 with the U.S. Department of Energy. The United States Government retains and the publisher, by accepting the article for publication, acknowledges that the United States Government retains a non-exclusive, paid-up, irrevocable, worldwide license to publish or reproduce the published form of this manuscript, or allow others to do so, for United States Government purposes. The Department of Energy will provide public access to these results of federally sponsored research in accordance with the DOE Public Access Plan (`https://www.energy.gov/downloads/doe-public-access-plan`).

Data used to generate figures can be obtained in the digital format by following the link in Ref. [56].

[1] T. C. Hender, J. C. Wesley, J. Bialek, A. Bondeson, A. H. Boozer, R. J. Buttery, A. Garofalo, T. P. Goodman, R. S. Granetz, Y. Gribov, et al., Nucl. Fusion **47**, S128 (2007).

[2] A. H. Boozer, Physics of Plasmas **22**, 032504 (2015), https://doi.org/10.1063/1.4913582, URL `https://doi.org/10.1063/1.4913582`.

[3] N. Commaux, L. Baylor, T. Jernigan, E. Hollmann, P. Parks, D. Humphreys, J. Wesley, and J. Yu, Nuclear Fusion **50**, 112001 (2010), URL `https://doi.org/10.1088%2F0029-5515%2F50%2F11%2F112001`.

[4] M. Lehnen, K. Aleynikova, P. Aleynikov, D. Campbell, P. Drewelow, N. Eidietis, Y. Gasparyan, R. Granetz, Y. Gribov, N. Hartmann, et al., Journal of Nuclear Materials **463**, 39 (2015), ISSN 0022-3115, pLASMA-SURFACE INTERACTIONS 21, URL `http://www.sciencedirect.com/science/article/pii/S0022311514007594`.

[5] E. M. Hollmann, P. B. Aleynikov, T. Fülöp, D. A. Humphreys, V. A. Izzo, M. Lehnen, V. E. Lukash, G. Papp, G. Pautasso, F. Saint-Laurent, et al., Physics of Plasmas **22**, 021802 (2015), https://doi.org/10.1063/1.4901251, URL `https://doi.org/10.1063/1.4901251`.

[6] L. Baylor, S. Meitner, T. Gebhart, J. Caughman, J. Herfindal, D. Shiraki, and D. Youchison, Nuclear Fusion **59**, 066008 (2019), URL `https://doi.org/10.1088%2F1741-4326%2Fab136c`.

[7] L. Hesslow, O. Embréus, A. Stahl, T. C. DuBois, G. Papp, S. L. Newton, and T. Fülöp, Phys. Rev. Lett. **118**, 255001 (2017), URL `https://link.aps.org/doi/10.1103/PhysRevLett.118.255001`.

[8] L. Hesslow, O. Embréus, M. Hoppe, T. C. DuBois, G. Papp, M. Rahm, and T. Fülöp, J. Plasma Phys. **84**, 905840605 (2018).

[9] D. Shiraki, N. Commaux, L. Baylor, C. Cooper, N. Eidietis, E. Hollmann, C. Paz-Soldan, S. Combs, and S. Meitner, Nuclear Fusion **58**, 056006 (2018), URL `https://doi.org/10.1088%2F1741-4326%2Faab0d6`.

[10] A. N. James, E. M. Hollmann, and G. R. Tynan, Review of Scientific Instruments **81**, 10E306 (2010), https://doi.org/10.1063/1.3475710, URL `https://doi.org/10.1063/1.3475710`.

[11] L. Carbajal, D. del Castillo-Negrete, D. Spong, S. Seal, and L. Baylor, Physics of Plasmas **24**, 042512 (2017), https://doi.org/10.1063/1.4981209, URL `https://doi.org/10.1063/1.4981209`.

[12] P. Aleynikov, K. Aleynikova, B. Breizman, G. Huijsmans, S. Konovalov, S. Putvinski, and V. Zhogolev, in *Proc. of the 25th IAEA Fusion Energy Conference* (IAEA, Vienna, 2014), St. Petersburg, Russia, tH/P3-38.

[13] S. Konovalov, P. Aleynikov, K. Aleynikova, Y. Gribov, R. Ismailov, A. Ivanov, R. Khayrutdinov, D. Kiramov, M. Lehnen, V. Leonov, et al., in *Proc. of the 26th IAEA Fusion Energy Conference* (IAEA, Vienna, 2016), Kyoto, Japan, tH/7-1.

[14] J. Martín-Solís, A. Loarte, and M. Lehnen, Nuclear Fusion **57**, 066025 (2017), URL `https://doi.org/10.1088%2F1741-4326%2Faa6939`.

[15] C. Reux, V. Plyusnin, B. Alper, D. Alves, B. Bazylev, E. Belonohy, A. Boboc, S. Brezinsek, I. Coffey, J. Decker, et al., Nuclear Fusion **55**, 093013 (2015), URL `https://doi.org/10.1088%2F0029-5515%2F55%2F9%2F093013`.

[16] D. A. Spong, D. del Castillo-Negrete, L. C. Gomez, C. Lau, D. P. Brennan, C. Liu, C. Collins, C. Paz-Soldan, M. A. V. Zeeland, K. E. Thome, et al., in *Proc. of the 27th IAEA Fusion Energy Conference* (IAEA, Vienna, 2018), Ahmedabad, India, tH/P8-17.

[17] D. del Castillo-Negrete, L. Carbajal, D. Spong, and V. Izzo, Physics of Plasmas **25**, 056104 (2018), https://doi.org/10.1063/1.5018747, URL `https://doi.org/10.1063/1.5018747`.

[18] G. Papp, M. Drevlak, T. Fülöp, and P. Helander, Nuclear

Fusion **51**, 043004 (2011), URL https://doi.org/10.1088%2F0029-5515%2F51%2F4%2F043004.

[19] G. Papp, M. Drevlak, T. Fülöp, P. Helander, and G. I. Pokol, Plasma Physics and Controlled Fusion **53**, 095004 (2011), URL https://doi.org/10.1088%2F0741-3335%2F53%2F9%2F095004.

[20] C. Sommariva, E. Nardon, P. Beyer, M. Hoelzl, G. Huijsmans, D. van Vugt, and JET Contributors, Nuclear Fusion **58**, 016043 (2017), URL https://doi.org/10.1088%2F1741-4326%2Faa95cd.

[21] C. Sommariva, E. Nardon, P. Beyer, M. Hoelzl, G. Huijsmans, and JET Contributors, Nuclear Fusion **58**, 106022 (2018), URL https://doi.org/10.1088%2F1741-4326%2Faad47d.

[22] V. Izzo, E. Hollmann, A. James, J. Yu, D. Humphreys, L. Lao, P. Parks, P. Sieck, J. Wesley, R. Granetz, et al., Nuclear Fusion **51**, 063032 (2011), URL https://doi.org/10.1088%2F0029-5515%2F51%2F6%2F063032.

[23] Z. H. Jiang, J. Huang, R. H. Tong, T. T. Yang, Z. F. Lin, V. Izzo, C. H. Li, Y. F. Liang, X. Ye, Y. H. Ding, et al., Physics of Plasmas **26**, 062508 (2019), https://doi.org/10.1063/1.5100093, URL https://doi.org/10.1063/1.5100093.

[24] C. J. McDevitt, Z. Guo, and X.-Z. Tang, Plasma Physics and Controlled Fusion **61**, 024004 (2019), URL https://doi.org/10.1088%2F1361-6587%2Faaf4d1.

[25] Y. Liu, P. Parks, C. Paz-Soldan, C. Kim, and L. Lao, Nuclear Fusion **59**, 126021 (2019), URL https://doi.org/10.1088%2F1741-4326%2Fab3f87.

[26] L. Carbajal, D. del Castillo-Negrete, and J. J. Martinell, Physics of Plasmas **27**, 032502 (2020), https://doi.org/10.1063/1.5135588, URL https://doi.org/10.1063/1.5135588.

[27] D. Whyte, T. Jernigan, D. Humphreys, A. Hyatt, C. Lasnier, P. Parks, T. Evans, P. Taylor, A. Kellman, D. Gray, et al., Journal of Nuclear Materials **313-316**, 1239 (2003), ISSN 0022-3115, plasma-Surface Interactions in Controlled Fusion Devices 15, URL http://www.sciencedirect.com/science/article/pii/S0022311502015258.

[28] E. Nardon, A. Fil, P. Chauveau, P. Tamain, R. Guirlet, H. Koslowski, M. Lehnen, C. Reux, F. Saint-Laurent, and JET Contributors, Nuclear Fusion **57**, 016027 (2016), URL https://doi.org/10.1088%2F0029-5515%2F57%2F1%2F016027.

[29] E. Hollmann, N. Eidietis, J. Herfindal, P. Parks, A. Pigarov, D. Shiraki, M. Austin, L. Bardoczi, L. Baylor, I. Bykov, et al., Nuclear Fusion **59**, 106014 (2019), URL https://doi.org/10.1088%2F1741-4326%2Fab32b2.

[30] X. Tao, A. A. Chan, and A. J. Brizard, Phys. Plasmas **14**, 092107 (2007), https://doi.org/10.1063/1.2773702, URL https://doi.org/10.1063/1.2773702.

[31] J. R. Cary and A. J. Brizard, Rev. Mod. Phys. **81**, 693 (2009), URL https://link.aps.org/doi/10.1103/RevModPhys.81.693.

[32] J. R. Cash and A. H. Karp, ACM Trans. Math. Softw. **16**, 201 (1990), ISSN 0098-3500, URL http://doi.acm.org/10.1145/79505.79507.

[33] D. A. Humphreys and A. G. Kellman, Physics of Plasmas **6**, 2742 (1999), https://doi.org/10.1063/1.873231, URL https://doi.org/10.1063/1.873231.

[34] L. L. Lao, J. R. Ferron, R. J. Groebner, W. Howl, H. S. John, E. J. Strait, and T. S. Taylor, Nucl. Fusion **30**, 1035 (1990).

[35] F. M. Levinton, R. J. Fonck, G. M. Gammel, R. Kaita, H. W. Kugel, E. T. Powell, and D. W. Roberts, Phys. Rev. Lett. **63**, 2060 (1989).

[36] A. Pletzer and D. McCune, *Ntcc pspline module* (2010), URL https://w3.pppl.gov/ntcc/PSPLINE/.

[37] E. Hollmann, M. Austin, J. Boedo, N. Brooks, N. Commaux, N. Eidietis, D. Humphreys, V. Izzo, A. James, T. Jernigan, et al., Nuclear Fusion **53**, 083004 (2013), URL https://doi.org/10.1088%2F0029-5515%2F53%2F8%2F083004.

[38] P. Helander and D. J. Sigmar, *Collisional Transport in Magnetized Plasmas* (Cambridge: Cambridge University Press, 2002).

[39] C. W. Gardiner, *Stochastic Methods* (Springer-Verlag, Berlin, Heidelberg, 2004).

[40] C. F. F. Karney and N. J. Fisch, The Physics of Fluids **28**, 116 (1985), https://aip.scitation.org/doi/pdf/10.1063/1.865191, URL https://aip.scitation.org/doi/abs/10.1063/1.865191.

[41] S. P. A. Sauer, J. Oddershede, and J. R. Sabin, in *Concepts of Mathematical Physics in Chemistry: A Tribute to Frank E. Harris - Part A*, edited by J. R. Sabin and R. Cabrera-Trujillo (Academic Press, 2015), vol. 71 of *Advances in Quantum Chemistry*, pp. 29 – 40, URL http://www.sciencedirect.com/science/article/pii/S0065327615000027.

[42] M. Rosenbluth and S. Putvinski, Nucl. Fusion **37**, 1355 (1997), URL http://stacks.iop.org/0029-5515/37/i=10/a=I03.

[43] L. D. Landau and E. M. Lifshitz, *The Classical Theory of Fields* (Pergamon Press, 1971), 3rd ed.

[44] J. D. Jackson, *Classical Electrodynamics* (Wiley, 1962).

[45] E. Hirvijoki, J. Decker, A. J. Brizard, and O. Embréus, J. Plasma Phys. **81**, 475810504 (2015).

[46] M. Bakhtiari, G. J. Kramer, M. Takechi, H. Tamai, Y. Miura, Y. Kusama, and Y. Kamada, Phys. Rev. Lett. **94**, 215003 (2005), URL https://link.aps.org/doi/10.1103/PhysRevLett.94.215003.

[47] N. Metropolis, A. W. Rosenbluth, M. N. Rosenbluth, A. H. Teller, and E. Teller, The Journal of Chemical Physics **21**, 1087 (1953), https://doi.org/10.1063/1.1699114, URL https://doi.org/10.1063/1.1699114.

[48] W. K. Hastings, Biometrika **57**, 97 (1970), ISSN 00063444, URL http://www.jstor.org/stable/2334940.

[49] E. M. Hollmann, P. B. Parks, N. Commaux, N. W. Eidietis, R. A. Moyer, D. Shiraki, M. E. Austin, C. J. Lasnier, C. Paz-Soldan, and D. L. Rudakov, Physics of Plasmas **22**, 056108 (2015), https://aip.scitation.org/doi/pdf/10.1063/1.4921149, URL https://aip.scitation.org/doi/abs/10.1063/1.4921149.

[50] J. Connor and R. Hastie, Nuclear Fusion **15**, 415 (1975), URL https://doi.org/10.1088%2F0029-5515%2F15%2F3%2F007.

[51] S. Putvinski, P. Barabaschi, N. Fujisawa, N. Putvinskaya, M. N. Rosenbluth, and J. Wesley, Plasma Physics and Controlled Fusion **39**, B157 (1997), URL https://doi.org/10.1088%2F0741-3335%2F39%2F12b%2F013.

[52] A. Loarte, V. Riccardo, J. Martin-Solís, J. Paley, A. Huber, M. Lehnen, and JET-EFDA Contributors, Nuclear Fusion **51**, 073004 (2011), URL https://doi.org/10.1088%2F0029-5515%2F51%2F7%2F073004.

[53] J. Martín-Solís, A. Loarte, E. Hollmann, B. Esposito, V. Riccardo, FTU, DIII-D Team, and JET-EFDA Contributors, Nuclear Fusion **54**, 083027 (2014), URL https://doi.org/10.1088%2F0029-5515%2F54%2F8%2F083027.

[54] L. Hesslow, O. Embréus, O. Vallhagen, and T. Fülöp, Nuclear Fusion **59**, 084004 (2019), URL https://doi.org/10.1088%2F1741-4326%2Fab26c2.

[55] O. Embréus, A. Stahl, and T. Fülöp, J. Plasma Phys. **84**, 905840102 (2018).

[56] URL https://github.com/mbeidler3/RE_ConVsCol_NF_2020.